

<https://doi.org/10.1038/s41699-024-00521-5>

Impact ionization and the paradox of defects in transition metal dichalcogenide FETs



Rupali Verma , Utpreksh Patbhaje, Asif A. Shah , Aadil Bashir Dar & Mayank Shrivastava

For developing high-performance, reliable, and robust electronic devices, fundamental analysis of the hot carrier dynamics, high field transport, and electrical breakdown mechanisms in transition metal dichalcogenide field effect transistors is essential, which is largely unknown. In this paper, using a combination of electrical measurements, high-field spatial electroluminescence measurements, and theoretical models, it is presented that the impact ionization in MoS₂ is mediated via defects, i.e., assisted via defect-induced trap states. Several unique observations, such as threshold voltage left-shift, increased subthreshold slope, anticlockwise hysteresis in the output characteristics, and bias-dependent redistribution of the electric field, are recorded when biased in the impact ionization regime, which we discover is due to the field-dependent dynamic occupancy of the defect states. Finally, we confirm a unified mechanism of high field breakdown as a competition between avalanche breakdown and minority carrier injection-induced breakdown from the variation of spatial electroluminescence with the gate voltage.

Two-dimensional (2D) Transition Metal Dichalcogenides (TMD) promise ultra-fast and highly scaled devices in the next generation information processing electronics^{1–3}. However, promising device architectures like the GAA transistors⁴, hot electron transistors^{5,6}, and avalanche transistors^{7,8} require operation in the high field regime, avalanche regime, or very close to the breakdown regime in some cases. Therefore, a thorough understanding of the high-field phenomena like Impact Ionization (II) and avalanche breakdown in TMD FETs is crucial. Moreover, avalanche multiplication also forms the basis of other semiconductor technologies like IMPATT diodes, avalanche photodiodes (used in image sensors, LIDAR sensors, optical fiber communication, etc.)^{9–11}, and single-photon avalanche photodiodes (SPADs) in the emerging field of quantum technology to detect single photons for quantum computing, and communication applications^{12,13}. Promising advances in 2D TMD-based avalanche transistors¹⁴ and avalanche photodetection^{15–17} are a significant push towards the heterogeneous integration of logic circuits, optoelectronics, and quantum technology in future electronics¹⁸. However, it also necessitates understanding avalanche multiplication in the 2D atomic limit with enhanced Coulomb interaction among charge carriers and defects due to the quantum confinement and the significantly reduced dielectric screening¹⁹. It is also suggested that because the conduction and valence bands in TMDs are narrow in energy (narrower than the bandgap), impact ionization is not expected in 2D TMDs²⁰, yet it happens! Kang et al. demonstrated anisotropic impact ionization and critical electric field in the lateral and vertical

multilayer WSe₂ FETs²¹. Pak et al. demonstrated tuning the avalanche breakdown critical electric field and the impact ionization rate with the channel thickness, originating from the changing bandgap with the number of layers in MoS₂ FETs²². Kim et al. demonstrated ambipolar transport and avalanche multiplication as two competing mechanisms of electrical breakdown in multilayer WSe₂ devices using channel length modulation²³. However, these works fail to establish the mechanism of avalanche multiplication in TMDs in light of the concerns formerly mentioned. Trap-assisted inverse auger effect is suggested to cause impact ionization in TMDs at high fields²⁴; however, it has not been experimentally proven. Moreover, the reliability challenges associated with the defect-assisted impact ionization mechanism are unknown. In this paper, we employ rigorous electrical characterization and current transport mechanism analysis, with temperature dependence, to address the gaps mentioned in the understanding of high-field transport and avalanche multiplication in 2D TMDs. We also corroborate the observations using spatial high-field Electroluminescence (EL) mapping, which was employed for the first time to investigate the electric field distribution in the back-gated TMD FETs.

Results

Back-gated FETs on chemical vapor deposition (CVD) grown Bilayer (BL) MoS₂ on SiO₂/Si substrate are used in this work. The flake triangles are patterned and etched to form (rectangular) channels with uniform widths and thicknesses (BL) to minimize the device-to-device variability from the

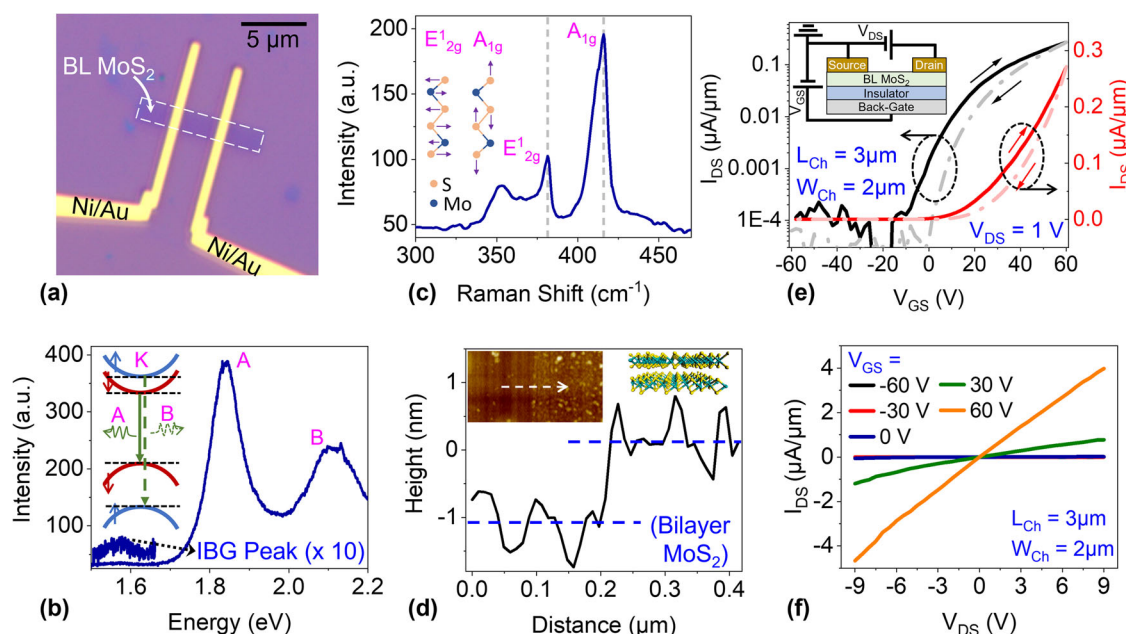


Fig. 1 | BL MoS₂ FET - Material and Device Characteristics. **a** Optical microscope image of a back-gated MoS₂ FET with Ni (30 nm)/Au (30 nm) contacts on Bilayer (BL) MoS₂ (marked in dashed white lines); Scale bar = 5 μm . Channel Length (L_{Ch}) = 3 μm , and Channel Width (W_{Ch}) = 2 μm . The CVD-grown BL MoS₂ was etched from the unwanted regions using O₂ plasma etching. **b** PL spectrum showing the A exciton, B exciton, and the 10 \times multiplied Indirect Bandgap (IBG) peaks.

c Raman spectrum in the channel region with the insets schematically presenting the origin of the observed peaks in the spectrum. **d** AFM topography line scan confirming the layer thickness to be of bilayer TMD. **e** $I_{\text{D}}-V_{\text{G}}$ confirms n-FET on BL MoS₂. The inset shows the schematic of the back-gate FET device structure. **f** The linear output characteristics of the device suggest a low metal-semiconductor Schottky barrier height at the contacts.

device dimensions (See Methods for more details). BL TMDs are advantageous for logic devices, providing good electrostatic control and higher mobility than monolayers²⁵. Figure 1a shows the optical image of a sample fabricated device. The Photoluminescence (PL) peak position²⁶ (Fig. 1b) and the peak position of the characteristic in-plane (E'_{2g}) and out-of-plane (A_{1g}) Raman modes²⁷ (Fig. 1c) confirm the chosen TMD to be MoS₂. The channel is established to be of bilayer MoS₂ from the AFM line scan (Fig. 1d), low energy indirect bandgap (IBG) peak (magnified in Fig. 1b), higher K-K direct bandgap than monolayer (ML) MoS₂ (Supplementary Fig. 1a), and the optical contrast differentiating the chosen flake from the ML on the growth substrate. The fabricated FETs show n-type characteristics (Fig. 1e). A low metal-semiconductor Schottky barrier is evident from the linear output characteristics ($I_{\text{D}}-V_{\text{D}}$) at 295 K (RT) in Fig. 1f. To further eliminate the effect of the device-to-device variability plaguing the 2D TMD devices²⁸, the FETs are biased in the sustainable breakdown regime by setting a current compliance level of 5 $\mu\text{A}/\mu\text{m}$ (refer to Supplementary Section A for more information) which ensured device recovery after high-field stress.

A sudden spike in the I_{DS} with V_{DS} indicates avalanche breakdown, and the decreasing critical breakdown voltage (V_{Cr}) with increasing gate voltage (V_{GS}) dependence confirms the electron injection-initiated impact ionization (Fig. 2a). The log plot in the inset shows current saturation with increasing bias below V_{Cr} , beyond which the slope of the $I_{\text{D}}-V_{\text{D}}$ curve rises rapidly with a dynamic on-resistance (R_{on}) till the current compliance level. High-field dielectric breakdown is ruled out as the gate current doesn't reach the compliance level (Supplementary Fig. 2).

The observed high-field breakdown was analyzed using the theoretical model for avalanche multiplication where the Multiplication factor ($M = I_{\text{DS}}/I_{\text{sat}}$; I_{sat} is the saturation current) is defined by ref. 29: $M = (1 - (V/V_{\text{B}})^n)^{-1}$. It can be rewritten in the linear form as $\ln(1 - 1/M) = n(\ln(V) - \ln(V_{\text{B}}))$, where n is the ionization index, and V_{B} is the critical voltage, which are fitting parameters. The linear fitting regime in the $\ln(1-1/M)$ vs. $\ln(V_{\text{DS}})$ in Fig. 2b confirms avalanche multiplication to be the cause of the unstable current at V_{Cr} . The extracted V_{B} and n decrease with increasing V_{GS} (Supplementary Fig. 3). While n (impact ionization index) was reported to be independent of V_{GS} earlier²³, we

observed a clear V_{GS} dependence. The calculated n value (range 6–16) is considerably higher than for silicon³⁰, confirming more efficient avalanche multiplication in MoS₂, possibly due to the quantum confinement and reduced dielectric screening, which increases the electron-hole interaction. Section B in the Supplementary information also confirms Fowler Nordheim Tunneling (FNT) of the electrons in the channel as the extrinsic source of electron injection for triggering impact ionization in the device (Supplementary Fig. 4a) where the effective FNT barrier height reduces with increasing V_{GS} (Supplementary Fig. 4b). The consistency of the electrical characteristics is confirmed in Supplementary Fig. 5. The V_{GS} dependence of n and V_{B} indicate either (i) decreasing size of the high field region (or depletion region) with increasing electrostatic n-doping, as a smaller depletion region ensures reaching the threshold field for impact ionization (E_{II}) at a smaller external voltage but also reducing the probability of ionizing collisions (and hence the impact ionization index n) in the region (Fig. 2c)³¹, or (ii) increasing n-doping reducing the impact ionization efficiency due to the electrostatic screening, or (iii) both.

With the increase in temperature, V_{Cr} increases irrespective of the V_{GS} (Fig. 2c), further confirming avalanche breakdown. However, with increasing temperature, the V_{Cr} saturates due to increasing thermionic emission of the carriers ($I_{\text{D}}-V_{\text{D}}$ plots in Supplementary Fig. 6). The V_{Cr} for avalanche breakdown increases with the temperatures due to the enhanced optical and acoustic phonon scattering, which decreases the average energy of the field accelerated carriers, increasing the E_{II} . However, while the impact ionization threshold voltage has a positive temperature coefficient, and FNT is a temperature-independent process, the thermionic emission across the Schottky barrier increases with temperature. The resulting temperature dependence of the breakdown I-V is a cumulative effect of the three factors.

Mechanism of impact ionization in TMDs

For developing devices with efficient avalanche multiplication, it is also essential to understand the fundamental process of impact ionization in the atomically thin 2D TMDs in light of the quantum confinement, reduced dielectric screening¹⁹, increased effective electron and hole mass^{32,33}, and a different band structure from conventional semiconductors²⁰. The BL MoS₂

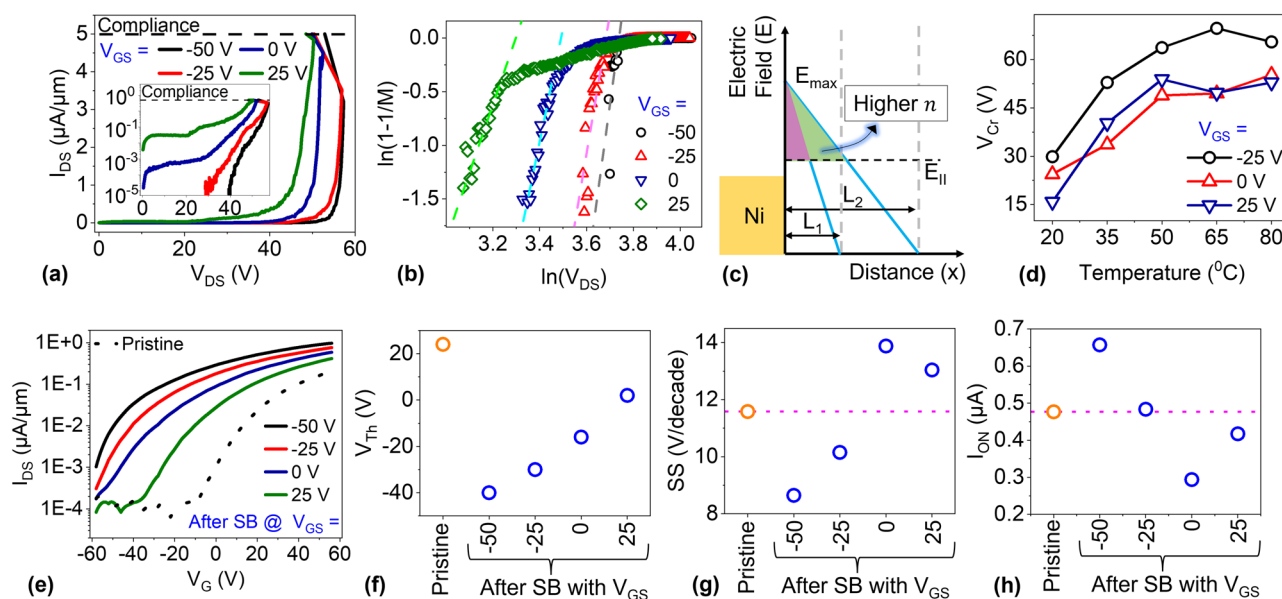


Fig. 2 | Electrical Breakdown Characteristics and FET parameter shifts. **a** Critical breakdown voltage V_{Cr} decreases with increasing electrostatic n doping. Log plot in the inset shows current saturation before the sudden rise with increasing V_{DS} . **b** Linear region in the $\ln(1-1/M)$ vs $\ln(V)$ plot indicating impact ionization in accordance with the empirical model. **c** For smaller depletion region width the maximum field exceeds E_{II} at smaller external voltage but the impact ionization

index is smaller. **d** Temperature dependence of V_{Cr} for varying V_{GS} indicating that the increase in V_{Cr} saturates with temperature and confirming impact ionization. **e** Change in the device I_D - V_G characteristics due to the V_{DS} sweep up to the current compliance for varying V_{GS} . **f** Negative V_{Th} shift magnitude decreases with increasing V_{GS} . **g** Variation in the SS, and **h** Variation in the ON current for constant over-drive voltage, from that of the pristine device.

band structure calculated using the Density Functional Theory (Supplementary Section C) in Supplementary Fig. 7 shows that the conduction bands are narrow in energy compared to the semiconductor bandgap. Therefore, to gain the threshold energy for impact ionization ($E_T \approx 1.5 \times E_G$), electrons must scatter (inter-valley and inter-band) and tunnel across bands multiple times – lowering the chances of impact ionization³⁴. The observation of NDC due to e's scattering to the higher energy and higher effective mass Σ valley (Supplementary Section D) suggests a further reduction in electron mobility. However, the observation of avalanche multiplication indicates that a few “lucky electrons” gain some threshold energy E_T associated with the mid-gap states^{35–38} in the lattice, resulting in the observation of impact ionization in the semiconductor.

Probing the Role of Defects in the Impact Ionization Process in TMD FETs. We recorded the device's transfer characteristics (I_D - V_G) before and immediately after the compliance current hit during the I_D - V_D avalanche soft breakdown (SB) sweep. For all applied V_{GS} , the I_D - V_G changes from the pristine behavior (Fig. 2e). To our best knowledge, all the previous reports on avalanche multiplication fail to report this effect on the electrical characteristics of TMD FETs post-SB, disregarding the effect of impact ionization on the device characteristics. A left threshold voltage (V_{Th}) shift is observed (Fig. 2f), with the magnitude decreasing with increasing V_{GS} (constant current method ($I_{DS} = 66$ nA) is used for the V_{Th} extraction³⁹). However, the subthreshold swing (SS) and the ON current variation do not align with the V_{Th} shift (Fig. 2g, h). It is important to note that the device I_D - V_G recovers with time (V_{GS} -dependent recovery data in Supplementary Fig. 9), ruling out the amorphization of the channel region⁴⁰ or the field-induced generation of defects⁴¹ as the origin of the shift. The Negative Bias Temperature Instability (NBTI) effect results in the left V_{Th} shift and an improved SS⁴² for negative V_{GS} . However, the degraded SS and reduced ON current (for the same overdrive voltage), with left V_{Th} shift for $V_{GS} = 0, 25$ V (semi-ON state), must be explored further.

To determine whether the change in the device characteristics is associated with the current instability due to the avalanche breakdown, we ramp the bias up in steps of 5 V (for $V_{GS} = 25$ V, with a dual sweep (DS)) and

investigate the evolution in the device I_D - V_G , recovering the device before the next sweep if any shift is noted (Fig. 3a). It is observed that below V_{Cr} , there is a non-significant change in the I_D - V_G , and the reverse sweep near traces the forward sweep; only a small clockwise hysteresis is visible in the log plot. The clockwise hysteresis results from trapping of the carrier in the lower mobility (Σ) valley during the reverse sweep because it only comes into effect over the range of V_{DS} where NDC is observed²⁴ and is absent for larger V_{DS} (Supplementary Fig. 10). However, as soon as the bias hits the V_{Cr} (critical voltage for avalanche multiplication), a significant anticlockwise hysteresis is noted⁴³. Simultaneously, in the I_D - V_G after DS (for $V_{DS} = 1$ V), degrading SS and left V_{Th} shift is observed (Fig. 3b). The consistency of the results is confirmed in Supplementary Fig. 11. For $V_{DS} = -1$ V (Fig. 3c), a continuous decrease in the n-branch of the I_D - V_G is also noted. After a high V_{DS} sweep with opposite polarity, the n branch in I_D - V_G decays for $V_{DS} = 1$ V (Supplementary Fig. 12). Irrespective of the V_{GS} , a similar effect was observed (Supplementary Fig. 13). The resulting mutation in the FET (i) reduces the V_{Cr} for positive V_{DS} , where anticlockwise hysteresis in I_D - V_D is also observed, and (ii) reduces I_{DS} for negative V_{DS} , highlighting the asymmetric effect of the impact ionization in the FET (Supplementary Fig. 14) - decrease in the Schottky barrier for electron injection at the source contact, and increase at the drain contact (Fig. 3d). Therefore, the asymmetric change in the Schottky barrier for electron injection is confirmed as the mechanism for the bipolar resistive switching observed in lateral TMD FETs⁴³.

A possible mechanism that we hypothesize for the left V_{Th} shift, degraded SS, and the anticlockwise hysteresis is the impact ionization of chalcogenide vacancy-induced deep donor states^{37,44–47} in MoS₂ near the source contact edge due to the defect-assisted impact ionization process. It is known that a depleted junction forms at the source contact for positive V_{DS} ^{48,49} and $V_{GS} > V_F$ (flat band voltage), which results in a localized high electric field in the channel. The high field on the source is confirmed by spatial photocurrent measurement (Fig. 3e), with maximum photoresponsivity reaching 10.2 A/W, when the laser ($P = 0.98$ μ W, $\lambda = 532$ nm, 50X objective) is illuminated on the source edge. The maximum photoresponsivity with minimum dark current is observed at V_{Cr} , where it can be biased for efficient avalanche photodiode applications. The mechanism

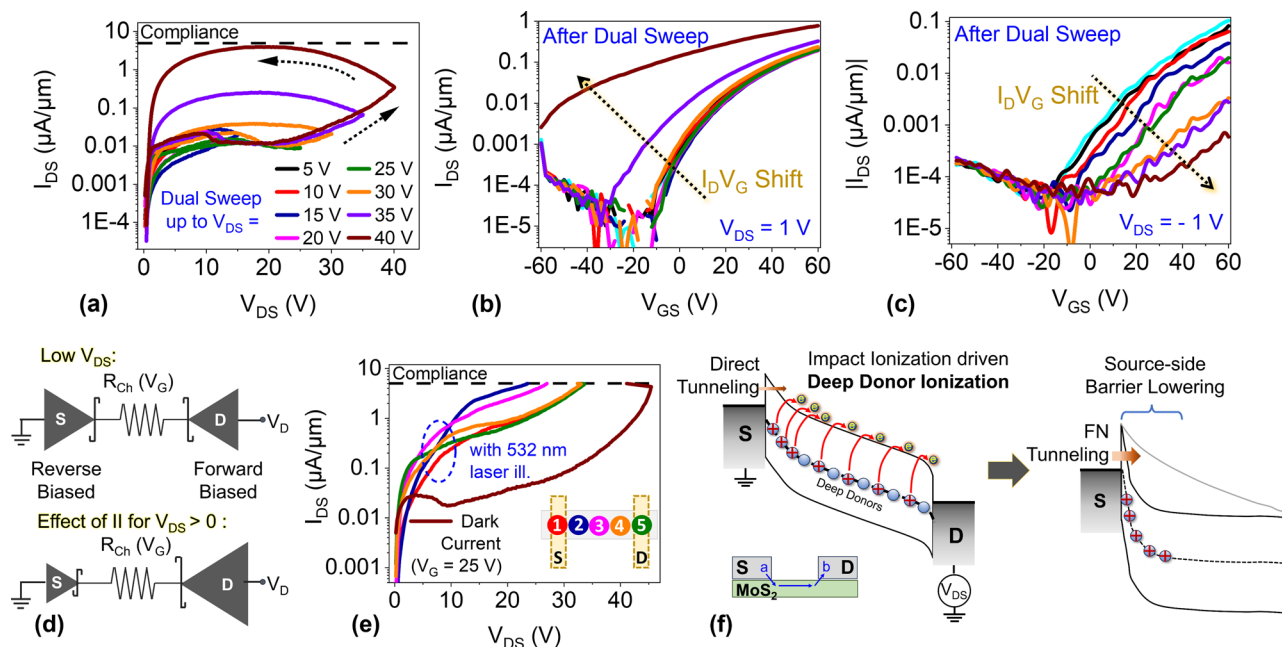


Fig. 3 | IdVd Anti-clockwise hysteresis and the Role of Defects. **a** I_D - V_D dual sweep (DS) with the end-point of the forward sweep increasing in steps of 5 V shows a significant hysteresis for bias beyond V_{Cr} . I_D - V_G of the device pre and post the bias sweep up to different voltages in the breakdown regime (**b**) for $V_{DS} = 1$ V shows a degrading SS and a left V_{Th} shift (**c**) for $V_{DS} = -1$ V shows a degrading SS and a right V_{Th} shift. **d** High field stress reduces the Schottky barrier at the source contact and increases the Schottky barrier at the drain contact. The Schottky barrier height

symbolized as the size of the diode in the schematic. **e** Spatial photocurrent mapping confirms higher electric field on the source edge than at the drain edge from the higher photocurrent with the laser illumination. **f** Schematic band diagram from point a to b in the inset device schematic, showing the mechanism of the source contact effective barrier lowering due to the high electric field induced local ionization of the deep donor levels, and its impact on the electric field distribution in the channel.

leading to the left V_{Th} shift due to the deep donor ionization from the impact ionization process is explained in Fig. 3f. Positive V_{DS} generates a high electric field on the source edge (reverse biased Metal-Semiconductor Schottky junction) impact ionizing the electrons from deep traps in the semiconductor and thereby reducing the effective barrier height due to the increased positive fixed charge concentration resulting from the ionization of sulfur vacancies. This results in the observed left V_{Th} shift and reduced V_{Cr} . The degraded SS results from (i) positive fixed charges that interfere with the gate modulation, (ii) change in the electric field profile, turning ON of the different regimes in the channel over a larger V_{GS} range, and (iii) vacancy-assisted electron hopping transport in the OFF and semi-ON bias condition⁵⁰. It is to be noted that we do not consider the inverse piezoelectric effect-induced degradation in the device characteristics because BL MoS_2 has a preserved inversion symmetry⁵¹. The anticlockwise hysteresis in the I_D - V_D results from the ionization of the electrons trapped in the sulfur vacancy sites at V_{Cr} , which lowers the source edge Schottky barrier responsible for electron injection. The increase in the drain edge Schottky barrier results from the accumulation of the electrons during ejection to the drain electrode. During the temporal recovery, the occupancy of the vacancy sites is restored to the equilibrium state.

Slew-rate dependence of the avalanche breakdown. The V_{Cr} decreases (Fig. 4a), and the left V_{Th} shift and SS degradation are enhanced due to the decreasing slew rate (Fig. 4b) of the I_D - V_D sweep. This further confirms the role of mid-gap states in the impact ionization process. The I_{sat} reduces for a smaller slew rate because of the increased phonon scattering. A smaller slew rate will increase the ionization of the mid-gap states, and therefore, the impact ionization process will also be affected. The FNT plots in Fig. 4c, for $V_{DS} > V_t$ (V_t : transition voltage from Direct Tunneling to FN Tunneling), can be fitted with two linear fitting regimes with different slopes (irrespective of the slew rate), indicating changing effective barrier height for FNT with the increasing bias. At the onset of FNT ($@V_t$), the effective electron barrier height is lesser for a smaller slew

rate (marked in oval shape) because of the increased defect state ionization on the source edge, which reduces the electron tunneling barrier width and results in reduced V_{Cr} . Supplementary Fig. 15 confirms the consistency of the observation. Also, the impact ionization index (slope of the linear fit in the $\ln(1-1/M)$ vs. $\ln(V)$ plot) is larger for a higher slew rate (Fig. 4d) because of the larger depletion region width (explained in Fig. 2c). The olive, blue, and magenta dashed lines in Fig. 4a, c, d define the different regimes in the breakdown current for slew rate = 1 V/s. Avalanche Multiplication (AM) of FN tunneled electrons is dominant from olive to blue dashed lines. Then, there is no AM (or AM with a small ionization index evident from the low slope linear fitting in Fig. 4d), and no FNT between the blue-magenta dashed lines. Beyond the magenta dashed line, the FNT transport dominates the AM-generated current. A transition from the AM to the FNT dominant regime occurs irrespective of the slew rate, albeit at different voltage ranges. We hypothesize that this dynamic evolution of the transport mechanism from AM to FNT results from the dynamic redistribution of the electric field in the channel with increasing lateral bias if the electric field is not uniformly distributed in the channel.

High field electroluminescence in TMD FETs. We also confirm the electric field redistribution resulting from the competition between the impact ionization of sulfur vacancies and the e^- -filling of the vacancy sites by FN tunneled electrons (due to non-uniform electric field distribution) from the spatial EL evolution with V_{DS} . For $V_{GS} = 25$ V, in the AM regime, the EL is first observed at the center of the channel, which shifts to the drain edge with increasing bias. EL migration possibly happens from the source to the drain edge, but the camera's sensitivity for lower current at lower bias limits the observation. The emission then diminishes, and with further increasing bias the intensity increases again on the drain edge. In the FNT regime, the EL intensity also initiates on the source edge (Fig. 4e). This increase, decrease, and increase of the EL intensity aligns with the AM to FNT transition observed in the I-V characteristics. The

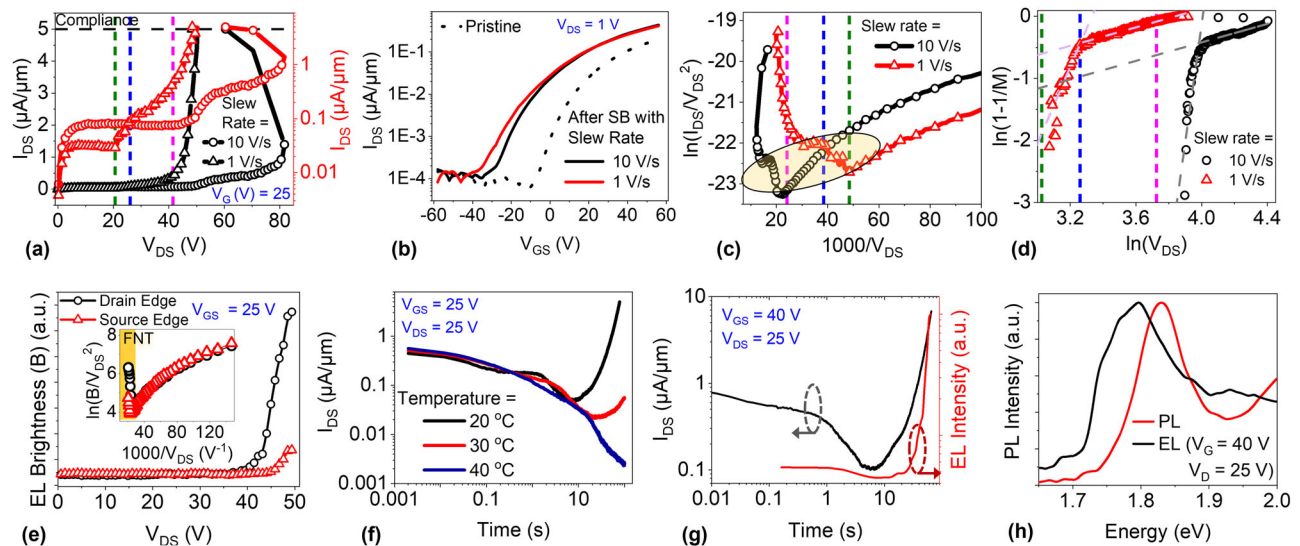


Fig. 4 | Slew Rate Dependent Electrical Breakdown and High Field Electro-luminescence. **a** Slew rate dependent breakdown, V_{Cr} and I_{sat} increase with the slew rate. **b** Larger negative V_{Th} shift (or a degraded SS) is observed from a smaller slew rate. The V_{Th} shift is found to be recoverable after every sweep. **c** FNT plot showing F-N tunneling current in the device in the breakdown regime of operation. **d** $\ln(1-1/M)$ vs $\ln(V_{DS})$ plot where the linear fitting suggests impact ionization in the bias regime. A higher ionization index is observed for larger slew. Olive, blue, and Magenta dashed lines in the plots mark different breakdown regimes in the device as

explained in the text. **e** V_{DS} dependent EL intensity at the source and the drain edge for $V_{GS} = 25$ V. **f** Temporal rise of I_{DS} shows a negative activation energy suggesting the role of hot carrier in the ionization of the deep donor levels. **g** The increase in the temporal current is accompanied by increase in the EL intensity. **h** The EL spectrum acquired for $V_{GS} = 40$ V shows low energy trion recombination dominating over excitonic recombination because of the high electrostatic n-doping. The trion recombination confirms K-K electron-hole pair generation and recombination in the impact ionization regime.

evolution of the EL with increasing source-drain voltage can be seen more clearly from the Supplementary Movie 1a (for $V_{GS} = 25$ V). In the AM regime, EL is observed in the localized high-field regions in the channel depending on the band-bending due to the applied V_{GS} (between olive and blue dashed lines (mentioned earlier)). The dependence of the EL brightness (B) on the applied bias in the inset also confirms FNT as the source of free carriers responsible for the observation of high-field EL (Fig. 4e inset). With the increasing bias, the electric field redistributes (reducing electric field in regions with localized high carrier concentration), dimming the free carrier source and lowering the ionization index due to the lower overall electric field (between blue and magenta dashed lines). Further increase in the bias enables FN tunneling of electrons from the source edge, which acts as the source of free carriers and results in the EL at the source edge (beyond the magenta dashed line). The large EL intensity at the drain edge is due to the high field from the junction termination effect when the field reaches the drain edge. In the OFF state at negative V_{GS} , EL was only observed at the drain edge with a consistent indication of AM to FNT transition (Supplementary Section D and Supplementary Movie 1 (b–d)).

The transient evolution of the drain current (Supplementary Section E) also unfolded the role of the impact ionization of the mid-gap defects in the observed left V_{Th} shift for positive V_{DS} (Supplementary Fig. 17a, b). Initially, the drain current decreases due to the Positive Bias Temperature Instability (PBTI) effect; however, the time-dependent ionization of the defect states eventually leads to the increase in I_{DS} . A strong V_{DS} dependence on the rise in the I_{DS} was also observed (Supplementary Fig. 17c). Most importantly, the defect emission showed an increasing emission time with temperature, indicating the role of hot electrons at the high electric field to be responsible for the impact ionization of the defect states (Fig. 4f). Supplementary Fig. 18 confirms further that the increasing emission time with temperature is not due to device degradation. The observation of negative activation energy indicates that due to the increased coulomb interaction (from quantum confinement and reduced dielectric screening), impact ionization dominates over thermal ionization or field-assisted Poole-Frenkel effect-induced ionization at high electric fields, which happens only at low temperatures in bulk semiconductors⁵². The high field current transient also shows

increasing EL intensity with the increasing current (Fig. 4g) due to the triggering of the non-Arrhenius impact ionization process with time. The EL spectrum for $V_{GS} = 40$ V (for enhanced EL emission to capture the spectrum) indicates trion recombination dominating over excitonic recombination in the ON state regime (Fig. 4h), which further confirms that the defect-assisted impact ionization process generates e/h pair in the CB/VB which recombine at the (higher energy, direct bandgap) K point in the Brillouin zone in the indirect bandgap semiconductor (BL MoS₂), emitting photons. The current instability is not merely due to Poole Frenkel emission of the defect states.

Unified electrical breakdown mechanism in 2D TMD FETs. While the observations establish the electrical breakdown mechanism for BL MoS₂ FET, they do not unify the mechanism for all TMDs with different (n or p) doping, material bandgap, and layer number-dependent bandgap variation. For this, we analyze the V_{GS} -dependent breakdown and the accompanying spatial EL distribution for BL MoSe₂ FETs. It is observed that for 2D TMD FETs having ambipolar I_D - V_G , the high-field electrical breakdown mechanism is different from that in the device with unipolar behavior. In the BL MoSe₂ FET, significant hole transport is observed at negative V_{GS} (I_D - V_G in Fig. 5a). It suggests that the hole injection from the drain edge of the device is favorable despite the dominant n-doping of the FET. Various factors are known to boost hole injection in 2D TMD Schottky barrier FETs: (i) smaller semiconductor bandgap, (ii) higher work-function contact metal, and (iii) fermi level pinning of metal fermi-level close to the valence band of the semiconductor. Owing to the favorable hole injection, it is observed that in BL MoSe₂ FET, the V_{Cr} decreases with V_{GS} (Fig. 5b) because of the reduction in the hole injection barrier with decreasing V_{GS} . This contrasts with MoS₂ FETs, where the V_{Cr} increases with the decreasing V_{GS} . While impact ionization was observed in BL MoS₂ FET, it was not observed for BL MoSe₂ FETs with the same device dimensions. This was because of the ambipolar nature of the FET, which allows hole injection with increasing V_{DS} before the field reaches E_{II} ²³. Moreover, the V_{GS} dependence of the EL observed in MoSe₂ FET with ambipolar characteristics significantly differs from that in MoS₂ FET. Figure 5c shows that when MoSe₂ FET is biased in the regime with

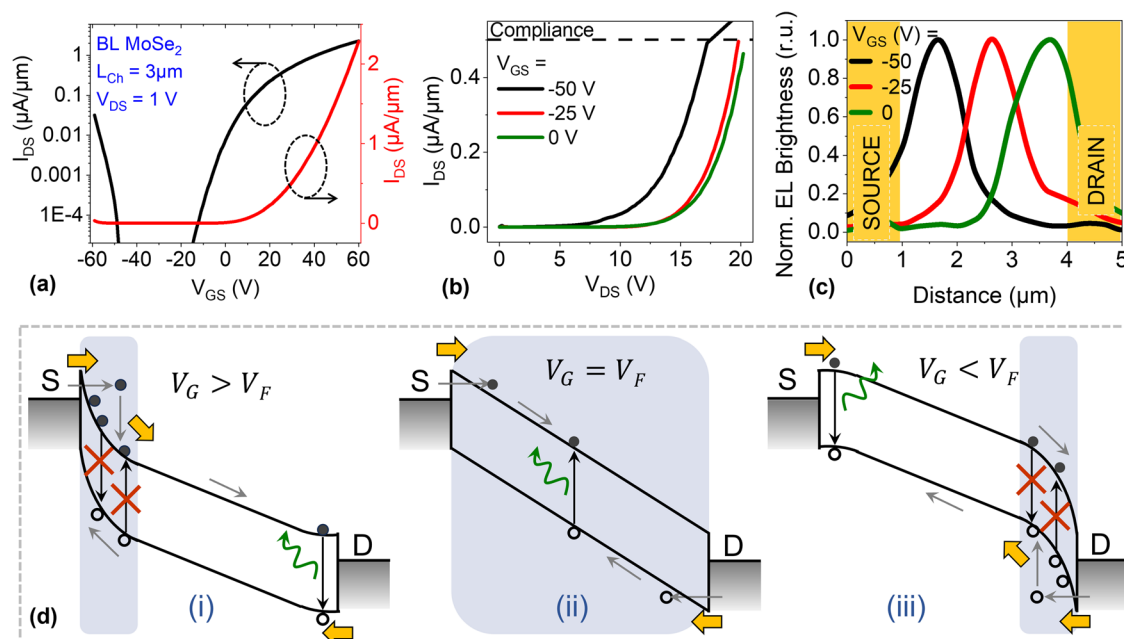


Fig. 5 | High Field Electrical Breakdown in Ambipolar TMD FETs. **a** I_D - V_G for BL MoSe₂ FET showing ambipolar behavior. **b** V_{CE} increases with V_{GS} , in contrast to the opposite observed for BL MoSe₂ FETs. **c** Spatial Distribution of EL in the breakdown

regime for varying V_{GS} in BL MoSe₂ FET. **d** Schematic showing the mechanism for EL in MoSe₂ FET at high enough V_{DS} for ambipolar carrier injection and varying V_{GS} . V_F means the flat-band voltage for the Schottky Barrier diode.

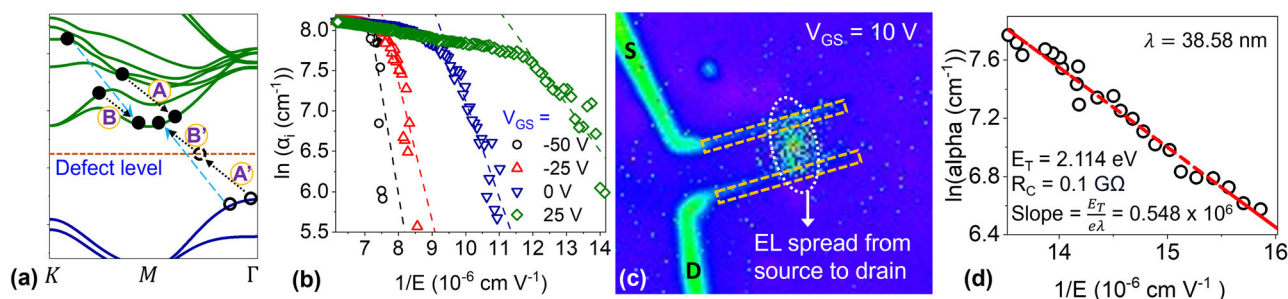


Fig. 6 | Defect Assisted Impact Ionization in BL MoS₂ FETs. **a** Possible transitions for impact ionization in semiconductors - blue arrows depict inverse Auger band-to-band impact ionization, and black arrows depict deep level defect assisted (A-A' + B-B') second order impact ionization process. **b** Electron α_i as a function of the inverse of the electric field indicating an increasing slope of the linear fitting with

decreasing V_{GS} . **c** EL uniformly spread across the channel for $V_{GS} = 10$ V. **d** Schockley model fitting for uniform EL distribution across the channel length: α_i vs inverse of the electric field; the electric field across the channel evaluated by subtracting the voltage drop due to the contact resistance (R_C), where R_C was evaluated for $V_{GS} = 10$ V from the Y-function method.

dominant hole conduction, high field EL is observed on the source edge. When biased in the regime with dominant electron conduction, EL is observed on the drain edge. When electron and hole injection from the source and drain contacts are equally probable because of the similar effective electron and hole mass in TMDs^[20], the injected e-h recombines at the center of the channel. The observation is due to the recombination of the majority carrier in the device with the injected minority carrier at high electric field, which can be understood more clearly from the schematic in Fig. 5d for the three discussed cases: (i) $V_{GS} > V_F$, (ii) $V_{GS} = V_F$, and (iii) $V_{GS} < V_F$, where V_F can be defined as the flat-band voltage or more precisely the V_{GS} allowing equal electron injection efficiency from the source edge and hole injection efficiency from the drain edge.

The observation, therefore, unifies the breakdown mechanism in 2D TMD FETs as a competition between the impact ionization induced and the ambipolar carrier injection-induced electrical breakdown in TMD FETs, which can be distinguished from the V_{GS} -dependent breakdown voltage and the spatial EL information. V_{GS} -dependent EL snapshots in FETs on exfoliated MoS₂ (Supplementary Fig. 19) also confirm that the observed EL is not due to the junction termination effect at the drain contact but defines the electric field profile in the channel.

Discussion

Evident from CB-VB recombination in the EL spectrum, impact ionization in MoS₂ can occur as a band-to-band inverse Auger process (blue arrows) or through a defect-assisted transition (black arrows: A-A' + B-B' transitions) (Fig. 6a). Therefore, while defects in the 2D lattice decrease the carrier mobility, they can also support the hot carrier phenomenon of impact ionization through the defect-assisted second-order transition - hence the "paradox" of defects. The defect-assisted process has no restrictions imposed by momentum conservation; therefore, the figure only shows one of the many possible impact ionization transitions. The defect-assisted process can become dominant in the TMDs due to (i) enhanced scattering of the electrons by the multiple bands within E_T above the CB edge and (ii) quantum confinement-induced increased coulomb interaction between electrons, holes, and defects. However, considering that the (i) sulfur vacancy defect level is closer to the CB than the VB^{35,36}, and (ii) in the lucky electron model, more hot electrons will be available for defect-to-CB transition, than for VB-to-defect transition, the dynamic change in the space charge field of the charged impurity centers with increasing bias may dynamically distort the electric field distribution in the device as confirmed in the text.

The V_{GS} dependent $I_D - V_D$ data also fits well with the Shockley model⁵³: $\alpha_i(E) = \alpha_0 \exp(-E_{no}/E)$, where α_i is the impact ionization coefficient of electrons which is a function of the applied electric field (E), and $E_{no} = E_T/\lambda$. Here, λ is the mean free path of the electrons and α is deduced from the multiplication factor (M) by $\alpha = 1/(L(1 - 1/M))$ assuming a uniform electric field in length $L = L_{Ch}$, and approximately equal electron and hole impact ionization coefficients²³. This is confirmed by the linear fit in $\ln(\alpha_i(E))$ vs $1/E$ plot (Fig. 6b and Supplementary Fig. 20a). However, the decreasing slope of the linear fitting (E_{no}) with increasing V_{GS} (Supplementary Fig. 20b) indicates either (i) decreasing size of the high field region (L), or (ii) an increasing mean free path of the electrons with increasing electrostatic n doping (because E_T is independent of V_{GS}). For an n-type Schottky barrier FET, the field is expected to become more spread for decreasing V_{GS} approaching the flat band condition⁵⁴. However, the screening effect can increase the mean free path of electrons with n-doping, indicating the role of impurity centers in the impact ionization process – especially in the quantum confinement regime in BL MoS₂.

However, because the field is not uniformly distributed in the channel for all V_{GS} , the fitting was more comfortably done for the case where the EL intensity is uniformly distributed across the channel in the impact ionization regime (Fig. 6c). We also estimate the phonon scattering limited mean free path of electrons in the device from the resultant fitting. For $V_{GS} = 10$ V, the electric field did not redistribute due to the impact ionization taking place over the entire channel. To estimate the electric field across the channel, we subtract the voltage drop at the contacts from the applied voltage: $V_{Ch} = V_{DS} - I_{DS}^*R_C$; R_C : total contact resistance. We use the Y-function method⁵⁵ to determine the contact resistance (Supplementary Fig. 21) and use the value at $V_{GS} = 10$ V to determine the channel electric field, $E = V_{Ch}/L_{Ch}$; L_{Ch} : Channel length = 3 μm . From the slope of the linear fit in the $\ln(\alpha_i(E))$ vs $1/E$ plot (in accordance with the Schockley “lucky electron” model), and $E_T = 2.114$ eV, the mean free path of the electrons is obtained equal to 38.58 nm. The threshold electron energy for impact ionization is calculated by $E_T = E_G((2 + \gamma)/(1 + \gamma))$; $\gamma = m_h/m_e$, where $E_G = 1.57$ eV is obtained from the PL spectrum, and γ is calculated from the DFT calculated BL MoS₂ band structure for electrons in Q valley and holes in Γ valley. Even with the possible overestimation of the contact resistance using the Y-function method⁵⁶, the calculated mean free path value is unrealistic⁵⁷. This confirms a lower E_T , possibly belonging to the defect assisted process for impact ionization in MoS₂ (also indicated by the V_{GS} dependence of the α_i ; indicating increasing mean free path of electrons with increasing n-doping).

In conclusion, this work analyses the crucial role of defects in the electrical breakdown mechanism in 2D TMD based FETs. It highlights the fundamental limitation for impact ionization in MoS₂ imposed by the material band-structure and the role of defect states in facilitating a defect-assisted second order impact ionization process. The observation of anti-clockwise I_{DS} - V_{DS} hysteresis, left V_{Th} shift, increased subthreshold slope, and the slew-rate and gate voltage dependence of the breakdown confirm the role of defects in the breakdown mechanism while also indicating the reliability challenges associated with the defect enabled hot-carrier process. The non-Arrhenius temporal breakdown manifested due to the increased carrier-defect interaction in the 2D quantum confinement regime confirms the role of hot carriers in the breakdown process. The spatial and spectral distribution of the high field electroluminescence are revealed as an indispensable characterization method to determine the electric field distribution in different FET operating regimes, and to distinguish avalanche breakdown from ambipolar injection induced breakdown in TMD FETs. The observations in this study serve as a stepping stone for the development of robust next generation 2D electronics and optoelectronics, and for a reliable adoption of 2D device technologies based on avalanche phenomena.

Methods

Device fabrication

CVD-grown bilayer MoS₂ triangles on SiO₂/Si substrate were first patterned and etched into (rectangular) channels with uniform

dimensions = 2 μm \times 9 μm . This was accomplished by spin-coating bilayer PMMA 495 A4/ 950 A2 positive resist, e-beam lithography patterning of unwanted region in the triangular flake, MIBK: IPA (1:3) development and oxygen plasma etching in the Plasma Asher chamber for 40s at 20 sccm O₂ flow, RF Power = 20 W. Positive resist was used in the case instead of negative resist to prevent resist hardening induced contamination. The sample die was kept in acetone for 24 h after etching to remove all resist contamination from the desired flake region. Ni (30 nm)/Au (30 nm) contacts were deposited using e-beam lithography and e-beam deposition. The devices in the paper have a channel length (source-drain distance, L_{Ch}) = 3 μm , channel width (W_{Ch}) = 2 μm , oxide thickness of 285 nm, and contact length of 0.6 μm .

Measurement setup

All electrical measurements were carried out using 26XX Keithley SMUs in a Faraday cage-enclosed probe station in ambient. Unless mentioned otherwise, all the DC I-V sweeps were done with a slew rate of 1 V/s in steps of 0.2 V. The temperature-dependent measurements were done on the Linkam stage with a PID controller feedback loop to ensure a stable temperature at the set value during the measurements. The EL measurements were done by equipping the Optical Microscope with a high-sensitivity CCD camera with Peltier cooling from Andor Technology. For the best spatial EL resolution, a long working distance 100X objective was used to focus on the device area (additional 2X magnification from the microscope). The Raman and Photoluminescence measurements were done using a LABRam Horiba Spectrometer with 1800 and 600 grooves/mm grating, respectively.

Data availability

The data that support the findings of this work are available from the corresponding authors upon reasonable request.

Received: 28 July 2024; Accepted: 25 November 2024;

Published online: 24 March 2025

References

1. Lemme, M. C., Akinwande, D., Huyghebaert, C. & Stampfer, C. 2D materials for future heterogeneous electronics. *Nat. Commun.* **13**, 2–6 (2022).
2. Liu, C. et al. Two-dimensional materials for next-generation computing technologies. *Nat. Nanotechnol.* **15**, 545–557 (2020).
3. Katiyar, A. K. et al. 2D Materials in Flexible Electronics: Recent Advances and Future Prospectives. *Chem. Rev.* <https://doi.org/10.1021/acs.chemrev.3c00302> (2023).
4. Chen, Z. Gate-all-around nanosheet transistors go 2D. *Nat. Electron.* **5**, 830–831 (2022).
5. Lan, Y. W. et al. Dual-mode operation of 2D material-based hot electron transistors. *Sci. Rep.* **6**, 1–8 (2016).
6. Liang, B. W. et al. High-Frequency Graphene Base Hot-Electron Transistor. *ACS Nano* **15**, 6756–6764 (2021).
7. Björk, M. T., Hayden, O., Schmid, H., Riel, H. & Riess, W. Vertical surround-gated silicon nanowire impact ionization field-effect transistors. *Appl. Phys. Lett.* **90**, 142110 (2007).
8. Kim, M., Jeon, Y., Kim, Y. & Kim, S. Impact-ionization and Tunneling FET Characteristics of Dual-Functional Devices with Partially Covered Intrinsic Regions. *IEEE Trans. Nanotechnol.* **14**, 633–637 (2015).
9. Martyniuk, P. et al. Infrared avalanche photodiodes from bulk to 2D materials. *Light Sci. Appl.* **12**, 212 (2023).
10. Campbell, J. C. et al. Recent advances in avalanche photodiodes. *IEEE J. Sel. Top. Quantum Electron.* **10**, 777–787 (2004).
11. Campbell, J. C. Recent advances in avalanche photodiodes. *Opt. Fiber Commun. Conf. OFC* **25**, 109–121 (2015).
12. Fan-Yuan, G. J. et al. Optimizing Single-Photon Avalanche Photodiodes for Dynamic Quantum Key Distribution Networks. *Phys. Rev. Appl.* **13**, 1 (2020).

13. Ceccarelli, F. et al. Recent Advances and Future Perspectives of Single-Photon Avalanche Diodes for Quantum Photonics Applications. *Adv. Quantum Technol.* **4**, 2000102 (2021).
14. Choi, H. et al. A steep switching WSe₂ impact ionization field-effect transistor. *Nat. Commun.* **13**, 1–9 (2022).
15. Seo, J. et al. Ultrasensitive Photodetection in MoS₂ Avalanche Phototransistors. *Adv. Sci.* **8**, 1–9 (2021).
16. Jia, J. et al. Avalanche Carrier Multiplication in Multilayer Black Phosphorus and Avalanche Photodetector. *Small* **15**, 1–8 (2019).
17. Lei, S. et al. An atomically layered InSe avalanche photodetector. *Nano Lett.* **15**, 3048–3055 (2015).
18. Shrivastava, M. & Ramgopal Rao, V. A Roadmap for Disruptive Applications and Heterogeneous Integration Using Two-Dimensional Materials: State-of-the-Art and Technological Challenges. *Nano Lett.* **21**, 6359–6381 (2021).
19. Chernikov, A. et al. Exciton binding energy and nonhydrogenic Rydberg series in monolayer WS₂. *Phys. Rev. Lett.* **113**, 1–5 (2014).
20. Ferry, D. K. Electron transport in some transition metal dichalcogenides: MoS₂ and WS₂. *Semicond. Sci. Technol.* **32**, 085003 (2017).
21. Kang, T. et al. Anisotropy of impact ionization in WSe₂ field effect transistors. *Nano Conver.* **10**, 13 (2023).
22. Pak, J. et al. Two-Dimensional Thickness-Dependent Avalanche Breakdown Phenomena in MoS₂ Field-Effect Transistors under High Electric Fields. *ACS Nano* **12**, 7109–7116 (2018).
23. Kim, J. et al. Channel-Length-Modulated Avalanche Multiplication in Ambipolar WSe₂Field-Effect Transistors. *ACS Nano* **16**, 5376–5383 (2022).
24. He, G. et al. Negative differential conductance & hot-carrier avalanching in monolayer WS₂ FETs. *Sci. Rep.* **7**, 1–9 (2017).
25. Zhang, X. et al. Transition metal dichalcogenides bilayer single crystals by reverse-flow chemical vapor epitaxy. *Nat. Commun.* **10**, 598 (2019).
26. Pierucci, D. et al. Large area molybdenum disulphide- epitaxial graphene vertical Van der Waals heterostructures. *Sci. Rep.* **6**, 1–10 (2016).
27. Li, H. et al. From bulk to monolayer MoS₂: Evolution of Raman scattering. *Adv. Funct. Mater.* **22**, 1385–1390 (2012).
28. Lanza, M., Smets, Q., Huyghebaert, C. & Li, L. J. Yield, variability, reliability, and stability of two-dimensional materials based solid-state electronic devices. *Nat. Commun.* **11**, 1–5 (2020).
29. Chynoweth, A. G. Ionization Rates for Electrons and Holes in Silicon. *Phys. Rev.* **109**, 1537 (1958).
30. Miller, S. L. Ionization Rates for Holes and Electrons in Silicon. *Phys. Rev.* **105**, 1246 (1957).
31. Levinstein, M., Kostamovaara, J. & Vainshtein, S. Selected Topics in Electronics and Systems - Vol. 36. *Breakdown Phenomena in Semiconductors and Semiconductor Devices*. (World Scientific Publishing Co. Pte. Ltd., 2005).
32. Yoon, Y., Ganapathi, K. & Salahuddin, S. How good can monolayer MoS₂ transistors be? *Nano Lett.* **11**, 3768–3773 (2011).
33. Ramasubramaniam, A. Large excitonic effects in monolayers of molybdenum and tungsten dichalcogenides. *Phys. Rev. B Condens. Matter Mater. Phys.* **86**, 1–6 (2012).
34. Chynoweth, A. G. Chapter 4 Charge Multiplication Phenomena. *Semicond. Semimet.* **4**, 263–325 (1968).
35. Mitterreiter, E. et al. The role of chalcogen vacancies for atomic defect emission in MoS₂. *Nat. Commun.* **12**, 1–8 (2021).
36. Zhao, Y. et al. Electrical spectroscopy of defect states and their hybridization in monolayer MoS₂. *Nat. Commun.* **14**, 1–9 (2023).
37. Shang, J. et al. Revealing electronic nature of broad bound exciton bands in two-dimensional semiconducting W S₂ and Mo S₂. *Phys. Rev. Mater.* **1**, 1–10 (2017).
38. Kim, J. Y. et al. Experimental and theoretical studies of native deep-level defects in transition metal dichalcogenides. *npj 2D Mater. Appl.* **6**, 75 (2022).
39. Ortiz-Conde, A. et al. A review of recent MOSFET threshold voltage extraction methods. *Microelectron. Reliab.* **42**, 583–596 (2002).
40. Ansh, Kumar, J., Sheoran, G. & Shrivastava, M. Electrothermal transport induced material reconfiguration and performance degradation of CVD-grown monolayer MoS₂ transistors. *npj 2D Mater. Appl.* **4**, 37 (2020).
41. Ansh, A., Patbhaje, U., Kumar, J., Meersha, A. & Shrivastava, M. Origin of electrically induced defects in monolayer MoS₂ grown by chemical vapor deposition. *Commun. Mater.* **4**, 1–11 (2023).
42. Lim, D. et al. High performance MoS₂ field-effect transistor by hydrazine doping treatment. *Nanotechnology* **136805**, 136805 (2015).
43. Ansh & Shrivastava, M. Superior resistance switching in monolayer MoS₂ channel-based gated binary resistive random-access memory via gate-bias dependence and a unique forming process. *J. Phys. D. Appl. Phys.* **55**, 085102 (2022).
44. Rivera, P. et al. Intrinsic donor-bound excitons in ultraclean monolayer semiconductors. *Nat. Commun.* **12**, 871 (2021).
45. Shen, P. C. et al. Healing of donor defect states in monolayer molybdenum disulfide using oxygen-incorporated chemical vapour deposition. *Nat. Electron.* **5**, 28–36 (2022).
46. Greben, K., Arora, S., Harats, M. G. & Bolotin, K. I. Intrinsic and Extrinsic Defect-Related Excitons in TMDs. *Nano Lett.* **20**, 2544–2550 (2020).
47. Gelczuk, L. et al. Probing Defects in MoS₂ Van der Waals Crystal through Deep-Level Transient Spectroscopy. *Phys. Status Solidi - Rapid Res. Lett.* **14**, 1–6 (2020).
48. Guo, Y. et al. Field-effect at electrical contacts to two-dimensional materials. *Nano Res.* **14**, 4894–4900 (2021).
49. Wu, C. C. et al. Elucidating the photoresponse of ultrathin MoS₂ field-effect transistors by scanning photocurrent microscopy. *J. Phys. Chem. Lett.* **4**, 2508–2513 (2013).
50. Qiu, H. et al. Hopping transport through defect-induced localized states in molybdenum disulphide. *Nat. Commun.* **4**, 3–8 (2013).
51. Wu, W. et al. Piezoelectricity of single-atomic-layer MoS₂ for energy conversion and piezotronics. *Nature* **514**, 470–474 (2014).
52. Bernstein, J. B., Bender, E. & Bensoussan, A. The Correct Hot Carrier Degradation Model. *IEEE Int. Reliab. Phys. Symp. Proc.* **2023**, 1–5 (2023).
53. Shockley, W. Problems related to p-n junctions in silicon. *Czechoslov. J. Phys.* **11**, 81–121 (1961).
54. Li, H. M. et al. Metal-semiconductor barrier modulation for high photoresponse in transition metal dichalcogenide field effect transistors. *Sci. Rep.* **4**, 1–7 (2014).
55. Somvanshi, D., Ber, E., Bailey, C. S., Pop, E. & Yalon, E. Improved Current Density and Contact Resistance in Bilayer MoSe₂Field Effect Transistors by AlO_xCapping. *ACS Appl. Mater. Interfaces* **12**, 36355–36361 (2020).
56. Hemanjaneyulu, K., Kumar, J. & Shrivastava, M. Gaps in the Y-Function Method for Contact Resistance Extraction in 2D Few-Layer Transition Metal Dichalcogenide Back-Gated FETs. *IEEE Electron Device Lett.* **43**, 635–638 (2022).
57. Guo, R., Bu, X., Wang, S. & Zhao, G. Enhanced electron-phonon scattering in Janus MoSSe. *New J. Phys.* **21**, 113040 (2019).

Acknowledgments

The authors thank the Swarnjayanti Fellowship of the Department of Science and Technology for supporting this work. We thank Biswajeet Nayank and Prof. Prasana Kumar Sahoo from Indian Institute of Technology Kharagpur, India, for providing in-house-grown bilayer TMDs on SiO₂ on which all the experiments were conducted. The student authors Rupali Verma, Utpreksh Patbhaje, and Asif A. Shah also thank the Prime Minister's Research Fellowship (PMRF). The authors would also like to acknowledge the NNFC facility at CeNSE, IISc, for the fabrication support and the MSDLab for helpful insight and discussions.

Author contributions

R.V. fabricated the devices, performed electrical and electro-optic measurements, processed the data, analyzed the processed data and model fitting results, and wrote the paper. U.P. contributed to the data processing and analysis. A.A.S. contributed to the Quantum ATK generated bandstructures using DFT simulations. A.B.D. contributed in the fabrication of the devices used for the experiments. M.S supervised the research. All authors discussed the results and contributed to the writing of the manuscript.

Competing interests

The authors declare no competing interests.

Additional information

Supplementary information The online version contains supplementary material available at

<https://doi.org/10.1038/s41699-024-00521-5>.

Correspondence and requests for materials should be addressed to Rupali Verma.

Reprints and permissions information is available at

<http://www.nature.com/reprints>

Publisher's note Springer Nature remains neutral with regard to jurisdictional claims in published maps and institutional affiliations.

Open Access This article is licensed under a Creative Commons Attribution 4.0 International License, which permits use, sharing, adaptation, distribution and reproduction in any medium or format, as long as you give appropriate credit to the original author(s) and the source, provide a link to the Creative Commons licence, and indicate if changes were made. The images or other third party material in this article are included in the article's Creative Commons licence, unless indicated otherwise in a credit line to the material. If material is not included in the article's Creative Commons licence and your intended use is not permitted by statutory regulation or exceeds the permitted use, you will need to obtain permission directly from the copyright holder. To view a copy of this licence, visit <http://creativecommons.org/licenses/by/4.0/>.

© The Author(s) 2024